LARGE-SCALE WIND TUNNEL TESTING OF AN ADVANCED HYBRID LAMINAR FLOW CONTROL SYSTEM

P. Scholz*, A. Barklage*, B. van Rooijen†, A. Seitz‡, M. Horn§, C. Badrya*, R. Radespiel*
* TU Braunschweig, Institute of Fluid Mechanics, Braunschweig, Germany
† German-Dutch Wind tunnels (DNW), BU Large Low-Speed Facility (LLF), Marknesse, Netherlands
‡ German Aerospace Center (DLR), Institute of Aerodynamics and Flow Technology, Braunschweig, Germany
§ German Aerospace Center (DLR), Institute of Structures and Design, Stuttgart, Germany

Abstract

The present paper discusses the setup, data acquisition, some aspects of post-processing and exemplary data from a large-scale wind tunnel entry conducted in the DNW-LLF facility. The goal of the test was to verify the applicability of a novel, tailored skin, single duct (TSSD) suction system design for active laminar flow control. The model is a 1:0.7 scaled vertical tail plane (VTP) with a height of 4.45 m. The most important measurement methods are pressure scanning, mass flow metering and infrared imaging. The measured pressure is combined with CFD-data in a data-fusion process to reconstruct the full 3D pressure on the VTP surface despite the finite number of discrete pressure taps. This data in turn is used to predict the spatially resolved suction velocity distribution on the surface of the suction panel. Both methods, the pressure reconstruction and the suction velocity estimation, encompass a thorough uncertainty estimation and propagation. Also, the total suction mass flow is measured with a custom-designed metering system with a final accuracy of $\pm 0.1\%$ of the reading. The comparison with an integration of the suction velocity gives excellent agreement, raising confidence in all these methods.
This process, and the accompanying results of the detection of the transition line with infrared imaging, will be demonstrated for a symmetric flow case under reference conditions. A significant amount of laminar boundary layer flow was retained, demonstrating the general feasibility of the TSSD system.

Keywords

Laminar Flow Control; Wind Tunnel Experiments; Laminar-turbulent Transition

1. INTRODUCTION

The reduction of viscous drag with active laminar flow control (LFC) offers a very promising potential to increase the efficiency of large transport aircraft, [1].
Recently, *Karpuk et al.* [2] published aircraft design studies based on multi-disciplinary optimization (MDO) approaches, where they compared different approaches that could contribute to significant reductions in CO_2 emissions. On the level of MDO, they designed each configuration for a balance between equivalent CO_2 emissions and Direct Operating Costs (DOC). As based on their findings, LFC is expected to become the largest contributor to reduce CO_2 for future aircraft configurations, compared to e.g. ultra-high bypass ratio engines, advanced materials and structures and load alleviation.
LFC is being researched since several decades. The review articles of *Joslin* [3] and *Schrauf* [4] summarize the state-of-the-art of the 80s and 90s, the remaining challenges and list large-scale tests that were done until the turn of the century. An overview over the more recent developments can be found e.g. in [5] or in the comprehensive introduction of *Beck et al.* [1].

The very concept of LFC is to have a “suction plenum” underneath the actual surface, which is then covered with some sort of a micro-perforated surface. Generating a suitably low pressure in the plenum forces a flow through the perforated surface from the outer flow, i.e. from the lower regions of the boundary layer, into the plenum. On boundary layer level, this flow effectively appears as a (typically negative) wall-normal velocity at the wall. With this, the velocity profile of a laminar boundary layer can be influenced actively, which in turn allows to avoid unstable velocity profiles. Negative wall-normal velocities, or suction, respectively, are usually beneficial to all kinds of laminar boundary layer instabilities, e.g. Tollmien-Schlichting-modes, crossflow-modes and attachment line transition. Since for an airfoil the static pressure of the outer flow changes along chord, all LFC-systems require some way to either adjust the plenum pressure to the outer pressure (e.g. by means of several, small chambers in chordwise direction), or by varying the effective pressure-loss characteristics of the skin itself.
Without much doubt, the efficient and economical production of the micro-porous surface is one of the large

doi: 10.25967/570065

challenges yet unsolved. For wind tunnel or flight testing often micro-perforated metallic sheets produced by laser drilling have been used, e.g. [6], [7], and many others. However, laser drilling all suction panels of a full-scale transport aircraft seems infeasible (or at least uneconomical) and also suffers from other challenges, specifically the delicate reproducibility, which is important, because the geometrical shape of the holes and the associated pressure loss through the porous sheet has a large influence on the local suction velocity. This is even more true if seen for the full lifespan of a transport aircraft: The suction skin is a sensible element and in order to maintain the effect of the laminar flow control over the entire lifetime, the suction skin must be maintainable.

One approach to cope these challenges is the Tailored Skin Single Duct (TSSD) concept, originally published in [8] and [9]. The TSSD-system consist of a closed suction module, which in turn comprises an inner structure, stiffener ribs and the suction skin itself. A sketch of the elements for the TSSD-module used herein is shown in the right part of Fig. 1. This system in principle allows to mount/demount the suction-box as one, integral module, that could be maintained, repaired and calibrated without actually being mounted on the aircraft.

The TSSD-skin also establishes a concept for an economic fabrication, which can be industrialized and transferred to a large scale. Some details of the TSSD-skin are shown in the left part of Fig. 1. The skin consists of different layers of coarse-meshed metallic fabrics which are diffusion-welded to generate a porous, but self-supporting substrate. This is then covered by a close-meshed metallic fabric, which creates a desired–and designable–pressure loss so as to adapt the desired suction distribution to the outer pressure distribution. Finally, the metallic fabrics are covered with a 50 μm thick, metallic foil. The foil is treated with fine etching to generate a micro-perforation made of 50 μm holes. The shape of the holes is of high quality, e.g. with respect to the sharpness of the edges and the consistency of the diameter shape. Since the foil is thin, the pressure-loss characteristics of the holes are reproducible. The fine etching process is well established, industrialized, and a high production rate is feasible. At the same time, the surface quality is good enough to allow laminar flow.

The different steps for the design, development and verification of the TSSD-system have recently been summarized in [10]. The present paper will specifically give an overview over the studies done in the large-scale wind tunnel entry at the DNW-LLF facility. We will explain the experimental setup, data acquisition and some post-processing and also give a brief overview of the data that has been acquired. For one case, the VTP at symmetric flow under reference conditions, we will present all data required to rebuild the case. The paper will however not go into great detail with the interpretation of the data and discussion of several different flow cases and conditions. A thorough analysis and rebuilding of the cases will be a matter of future projects.

2. EXPERIMENTAL SETUP

2.1. VTP-model and TSSD suction panel

The basic model to carry the TSSD suction system for the wind tunnel test was an isolated vertical tail plane (VTP) model that has been used in several other wind tunnel entries for hybrid laminar flow control related tests, e.g. [11], [12]. The model has a span (i.e. height) of $b = 4.45$ m. The chord at the root is 4.91 m the chord at the tip is 2.22 m, leading edge sweep is $\Phi_{\mathrm{L/E}} = 40.4°$. The rudder hinge line is at 69 % of the local chord. Figure 2 shows a sketch of the model.

The VTP model was specifically designed to deliver boundary layer stability characteristics and boundary layer Reynolds numbers typical for an A320 VTP in cruise flight. To do so, the whole model is similar to an A320 VTP, but in a 1:0.7 scale, such that Reynolds number identity is achieved at a freestream velocity of 100 m/s in the wind tunnel. The airfoil thickness

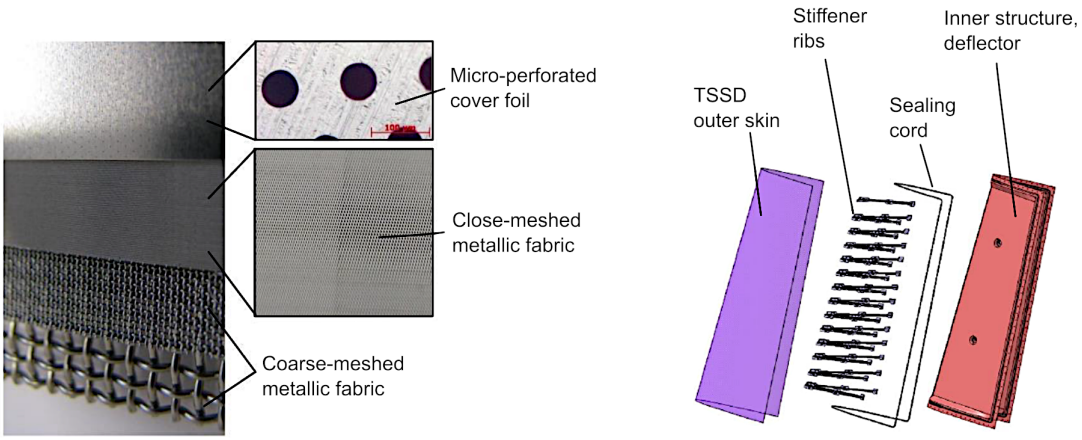

FIG 1. Concepts of the TSSD skin layout (left) and for the exchangeable suction module (right)

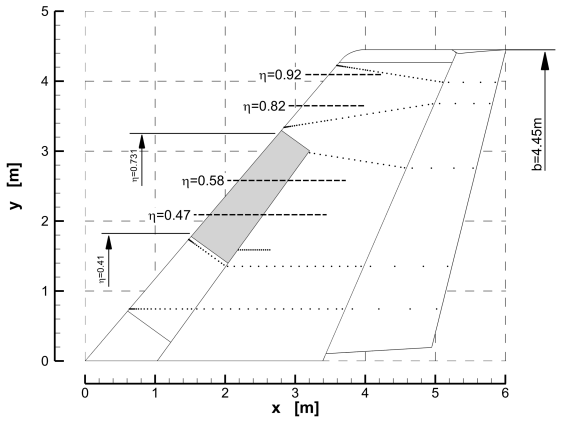

FIG 2. Side view of the model, including the location of the pressure taps. Four spanwise sections are highlighted that will be used in Sec. 3.

FIG 3. The VTP model in the test section of DNW-LLF, shown here with large sideslip angle for artistic reasons (Photo credits: DNW-LLF)

distribution was redesigned to compensate the lack of compressibility in the wind tunnel.
The suction panel for hybrid laminar flow control covers the region between $\eta = 0.41$ and $\eta = 0.731$ of relative span and reaches until $x/c = 0.19$ (in line-of-flight direction). The whole TSSD-system is basically one integral module that can be mounted into the leading edge. All transitions between the module and the backbone VTP model where filled, sanded and polished in the preparation.
The TSSD concept is a single-chamber system, i.e. only one single plenum exists underneath the microporous suction skin. Therefore, the main control parameter for the HLFC system is the plenum pressure coefficient $c_{P,p}$. In the model, the plenum pressure is measured in 36 different positions, 18 on both sides. The standard deviation of the individual plenum pressures is around $\sigma_{C_{P,p}} = 3.4\%$. Their mean value is used herein to quantify the strength of the suction. However, in the calculation for the local suction velocity, Sec. 2.3.2, the pressure distribution inside the plenum was actually taken into account. The plenum was also instrumented with temperature sensors to determine the density of the sucked air.
It is worth to note that the suction distribution was designed to maximize the laminar flow region, *not* taking into account the power required to drive the suction system. So the objective of this entry is not to operate the system at maximum efficiency, but to validate the feasibility of the TSSD skin.
To avoid attachment line transition from leading edge contaminations a custom-designed anti-contamination device (ACD) is mounted just below the suction panel. It is worth to note that the leading edge sweep Reynolds number is large enough to trigger attachment line transition. Therefore, the very leading edge region of the suction distribution is designed to reduce the momentum loss thickness of the attachment line boundary layer to $Re_\theta < 100$, ref. [10].

The model is equipped with a large number of static pressure taps in five different spanwise sections. The pressure taps are highlighted in Fig. 2.

2.2. Wind Tunnel and Measurement Methods

The model was tested in the 8 m $\times$ 6 m test section of the large low-speed facility (LLF)[1] of DNW in Marknesse, the Netherlands. The majority of tests was done at a freestream velocity $u_\infty = 100$ m/s, which is the design case for the VTP.
The model was mounted on a rotation table which in turn was connected to the six-component external underfloor balance. All moments and forces were recorded, however, since the focus of the entry was more on the transition position and only some part of the whole VTP is covered by the HLFC panel, the integral forces are not of major importance within this publication.
Beside scanning of static pressures the main measurement method was thermographic imaging of the model surface to measure transition positions. A total of four infrared cameras were installed: Two to monitor the port side and two for the starboard side. On each side of the model one camera observed the region behind the suction panel and one camera observed a region well upwards of the suction panel, where the flow over the VTP surface is not influenced by the suction. The latter region is the NLF-panel, which is used to monitor symmetry of the transition positions and to allow an exact N-factor calibration for this specific wind tunnel entry (or for each test point, if required). Fig. 4 provides an overview of the layout for the IR cams.
The infrared imaging requires a temperature difference between the surrounding air flow and the model structure, such that the different heat transfer coefficients of laminar and turbulent flow can lead to different model surface temperatures, which are recorded with the IR cams. The VTP model features in-built surface heating mats on both sides behind the HLFC panel and on the NLF-panel. In our case, however,

[1] https://www.dnw.aero/wind-tunnels/llf/

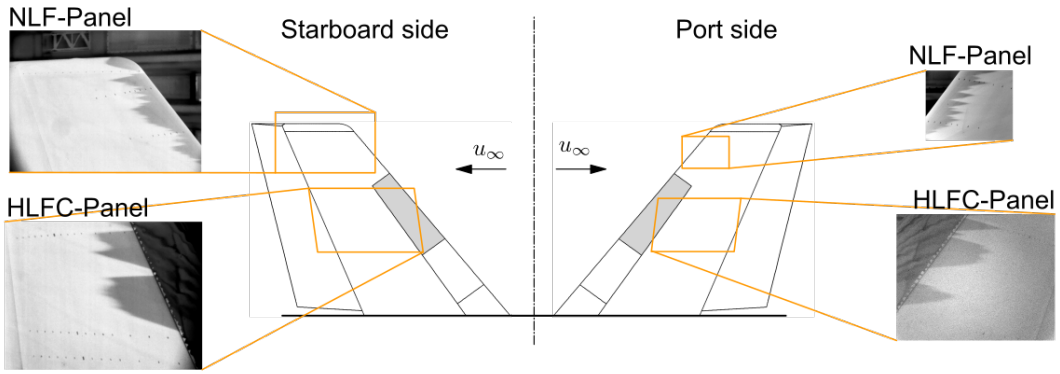

FIG 4. Layout of the infrared cameras to oberserve the NLF- and the HLFC-panels on both sides of the VTP

the naturally occurring slow heating of the wind tunnel flow was quite sufficient to produce an adequate temperature gradient and thus well visible transition lines. Therefore, the heating mats were effectively not used in this measurement.

Also, the infrared imaging requires a surface with low thermal conductivity, such that the surface temperature differences are reasonably sharp. The VTP body is made of fibre reinforced plastics coated with gelcoat, which gives a good contrast and, thus, allows high-quality IR images. This is not given on the metallic surface of the suction panel. As a consequence, the transition position can only be measured, if it is beyond the suction panel, i.e. $x_{Tr.}/c > 0.19$.

The majority of test cases were dedicated to generate a database for different angles of sideslip in the range $\beta = \pm 2°$, different rudder angles in the range $\delta_R = \pm 2°$, each with different strength of the HLFC suction $c_{p,P}$ and also some cases with smaller flow velocities. Most of these cases were also repeated inversely, i.e. a case $\beta = +2°$ and $\delta_R = -2°$ was repeated as $\beta = -2°$ and $\delta_R = +2°$ to identify asymmetries and uncertainties. In the present paper we will focus on the reference case, which is the one with symmetric flow conditions, $\beta = 0°$ and $\delta_R = 0°$ at $u_\infty = 100\,\text{m/s}$ and $Re = 22 \cdot 10^6$.

2.3. Mass Flow Metering and Suction Velocity Distribution

The most important parameters of the BL suction system are the total mass flow rate and the local suction velocity, both being related to each other. In the present wind tunnel entry both quantities were determined independently with different approaches, also including a thorough uncertainty quantification, [13], [14].

2.3.1. Direct mass flow measurement

The total mass flow rate can, in principle, be measured straightforward with a mass flow meter. Several physical principles to meter mass or volume flow rate are known. The device ultimately used herein was found in a comprehensive analysis and selection process, where the properties of different metering concepts were compared against the specific requirements of an HLFC wind tunnel test. The considered metering concepts were: laminar flow meters, rotary meters, turbine gas meters, ultrasonic or Coriolis meters, vortex flow meters, critical nozzles and calorimetric approaches. The selection was guided by a formal multi-criteria decision making method (weighted sum model), which finally gave the following ranking:

- Most important: Accuracy
- Medium importance: low risk (e.g. being “foolproof” and stable)
- Some relevance: Response time, practicability (e.g. mobility, complexity of the handling, required installation time) and generation of disturbances
- Minor relevance: Price, pressure losses in the meter, dynamic range, sensitivity to disturbances

The outcome of this process was finally that a combination of two rotary flow meters in a parallel arrangement is the most accurate, yet practical and extremely robust choice. Therefore, two identical rotary gas meters of type “FMR G250” were used as the backbone of the metering system.

The rotary flow meters require additional instrumentation to determine the density (pressure sensors Keller 30 PA A-33X and temperature sensors PT-100, class A). The whole setup was analysed with an uncertainty propagation method, which showed that the accuracy of the additional sensors, and therefore the accuracy of the density, is an order of magnitude better than the precision of the rotary meters. In other words, the accuracy of the system is dominated by the calibration of the rotary meters. Therefore, as a finally step, the whole system was calibrated against a calibration normal (critical nozzles) at the german national metrology institute PTB[2]. The rotary flow meters featured small, but measurable systematic deviations from the calibration normal that were finally eliminated by a non-linear calibration function.

The mass flow measured with this system will be denoted $\dot{m}_m$ in the following. It has a final accuracy of $\pm 0.1\%$ of the reading.

[2] https://www.ptb.de/cms/en/ptb/fachabteilungen/abt1/fb-14/ag-143.html

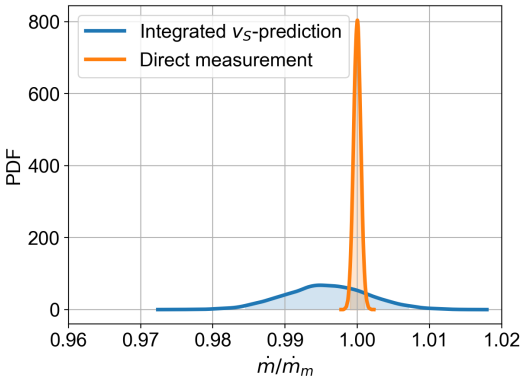

(a) Probability distributions of the mass flow rates measured directly with the meter, $\dot{m}_m$, and as a result of the v_S-prediction method

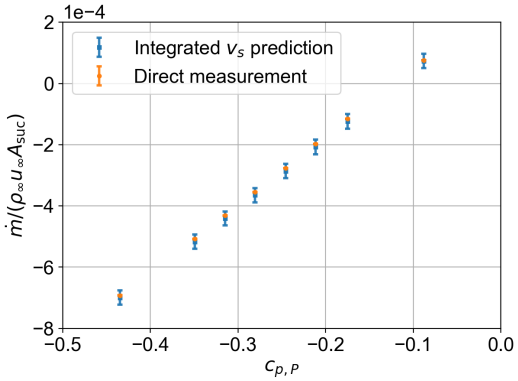

(b) Mass flow for different plenum pressures $c_{p,P}$ for the case $Re = 22 \cdot 10^6$, $\beta = 0°$, $\delta_R = 0°$

FIG 5. Comparison of the two different methods to determine suction mass flow rate

2.3.2. Suction velocity distribution

While for control purposes, both, the plenum pressure $c_{p,P}$ and the mass flow rate are suitable, for a re-building and deeper analysis the suction velocity distribution $v_S(x, y)$ is usually required. This is a challenging problem, because the flow rate through the micro porous sheet is basically a function of the pressure difference between the surface pressure on the outside c_p and the plenum pressure $c_{p,P}$. The surface pressure c_p however cannot be measured directly on the suction skin, but only in the static pressure tap sections below and above the suction panel. Furthermore, to determine the local suction velocity requires detailed and exact knowledge about the (local) pressure loss characteristics of the suction skin.
To solve this, a data-fusion approach was used in the present setup, including a thorough uncertainty analysis. The details of this method are published in [13] and [14], but will briefly be repeated:
The data fusion method is based on a Surrogate-Modelling Aero-Data Toolbox (SMARTy), [15], to fuse the experimental data (pressure distribution measured with several, but discrete and fixed pressure taps) with RANS simulation results of the VTP. The outcome of this process is the spatially resolved outer surface pressure c_p on the whole VTP, including the suction panel.
The local suction velocity is then determined from the pressure difference over the suction panel surface with a Darcy-Forchheimer equation for flow through a porous medium:

$$v_S = \frac{A \pm \sqrt{A^2 + 4B\,(c_p - c_{p,P}) \cdot q_\infty}}{2\,B} \tag{1}$$

In this equation, A and B are parameters that stem from the Darcy and Forchheimer terms. These parameters were calibrated in a preparative bench-top experiment with the actual TSSD-panel assembly, by measuring the local flow rate through the suction skin (for given plenum pressure $c_{p,P}$) with a probe, which is not unlike a small plunger. All elements on the right hand side of (1), except q_∞, are actually local values (x, y) coming from either the calibration step or the data fusion.
Since all of these values are also subject to uncertainties, the method is based on a probabilistic description of all input parameters. This also includes the effect of surface perturbations and the associated uncertainty of the outer pressure that might come from waviness or dents in the suction surface. The actual waviness and the "true" outer shape of the TSSD-surface is known from 3D laser scanning and is taken into account. Furthermore, the uncertainty of the data fusion itself, and accuracies of all individual sensors used during the process are included. The probabilities were then propagated using a Monte-Carlo method.
The final outcome of this process is a pressure distribution over the VTP and over the suction panel and a distribution of the (estimated) suction velocity on the panel, both including uncertainty bounds. Some results will be shown in Sec. 3.

2.3.3. Consistency of suction velocity and mass flow measurement

The local suction rate v_S can be integrated (including uncertainties) and should then equal the mass flow rate measured with the gas meters $\dot{m}_m$. The result of such a comparison is shown in Fig. 5(a). The PDF visualizes the uncertainty range of the two methods. As discussed above, the direct measurement has a narrow uncertainty band with a 95% credibility of $1.96 \cdot \sigma_{\dot{m}_m} = 0.001$, or 0.1% of $\dot{m}_m$, respectively. Although the uncertainty range for the prediction based on an integration of the local suction velocities is noticeably wider, the expected accuracy is better than 1 %–which, even for some of the direct metering concepts, would actually be quite a good accuracy. The two methods agree within the uncertainty bounds of the prediction, raising confidence that the local suction velocity distribution is reliable. Note that this level

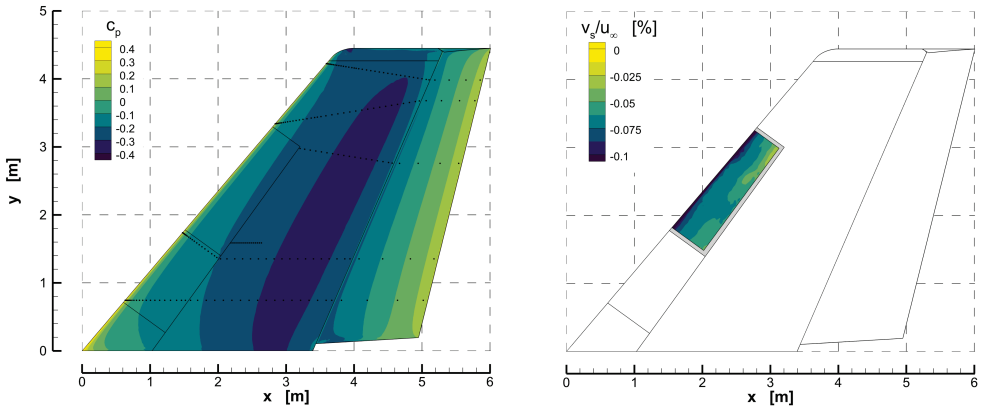

FIG 6. Result of the data fusion and v_s-prediction method: spatially resolved data for c_p and v_s.

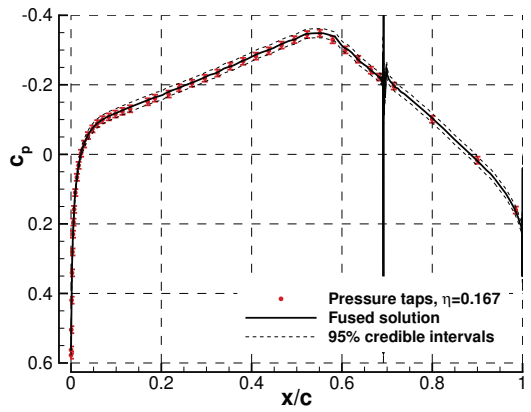

FIG 7. Comparison between fused solution and direct measurement in the lowermost pressure section $\eta = 0.167$.

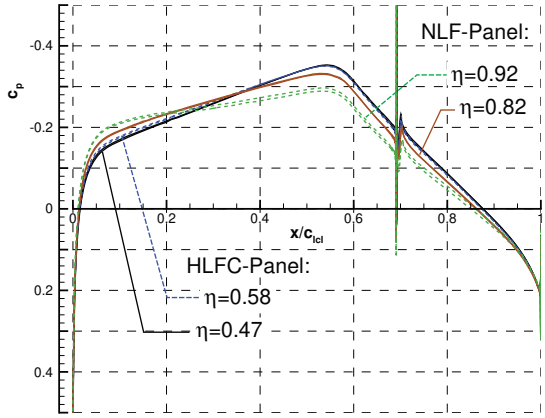

FIG 8. Pressure distributions in different sections for the reference case $\beta = 0°$, $\delta_R = 0°$ at $Re = 22{\cdot}10^6$.

of agreement was persistent for all data points in the whole wind tunnel entry. In general, the direct measurement was slightly larger than the expected value coming from the v_S-prediction. This indicates that there is some remaining, systematic influence. However, since the agreement is generally excellent we did not pursue this further.

Fig. 5(b) visualizes the total suction mass flow as a function of the plenum pressure $c_{p,P}$, again for both metering methods, for the symmetric flow case at reference conditions. It is clear that smaller plenum pressure gives more mass flow. Here, we label a "suction mass flow" with a negative $\dot{m}$. Again, the general agreement between the two methods is excellent. From this plot it becomes evident that too large plenum pressure actually generates a positive mass flow. As will be shown later, the minimum pressure on the outside of the suction panel is $c_p = -0.21$ for this case. So for all plenum pressures $c_{p,P} > -0.21$ we have to expect a local mass flux from inside the plenum into the outer flow, i.e. a "transpirating mass flow". For $c_{p,P} > 0.1$ not only some local transpiration is evident, but the total mass flow becomes positive. Of course, such cases are of little interest for laminar flow control. However, it gives even more confidence into the v_S-prediction that such cases with mixed suction and transpiration seem to agree very well with the direct mass flow measurement.

3. RESULTS

As said above, herein we will focus on the symmetric flow case $\beta = 0°$ and $\delta_R = 0°$ at reference conditions $u_\infty = 100$ m/s and $Re = 22 \cdot 10^6$.

The result from the data fusion and v_s-prediction method [14] is a spatially resolved c_p-distribution on the full VTP and also spatially resolved v_s-distribution on the suction panel. Such a result is shown in Fig. 6 as an example. The pressure distribution is relatively smooth, because it basically stems from the smooth results of a CFD simulation that has been fitted to the data measured with the actual pressure taps. A direct comparison between the fused data and the actually measured data can be done in the pressure sections, where the model is equipped with pressure taps. For the sake of brevity we only show the results of the lowermost pressure section, which is located at $\eta = 0.167$, in Fig. 7. In general, the fused solution is

an excellent representation of the actually measured data (not only in this section, but also for all others, where it can be checked). The contour lines in Fig. 6 qualitatively show, that the pressure isolines are *not* parallel to the leading edge. Hence, the results are more detailed than what could be achieved with the more straightforward approach to linearly interpolate between neighbouring pressure sections.

Fig. 6 also shows the predicted v_s-distribution on the suction panel, merely to recall that also the suction distribution is available on the whole surface, where suction is actually applied. In contrast to the pressure, the suction velocity distribution is less smooth. This comes from the fact that the suction skin parameters A and B, eqn. (1), measured in the bench-top experiment were a bit wavy and showed some inhomogeneity. It is worth to note that the parameters and the resulting suction velocity in the bench-top experiments were repeatable; it is therefore a deterministic property of the skin and not an uncertainty or inaccuracy.

For a more quantitative analysis we will focus on four different sections, that is $\eta = 0.47$ and 0.58 on the HLFC-panel and $\eta = 0.82$ and 0.92 on the NLF-panel, which are also indicated in Fig. 2. Furthermore, we will focus on analysis in sections of constant span, i.e. “line-of-flight” sections. The pressure distribution in the four sections for the symmetric case at reference conditions is given in Fig. 8. To be very precise, the data shown here is taken from the case with maximum suction rate, i.e. $c_{p,P} = -0.434$. However, the pressure distribution is effectively not influenced by the suction rate. As can be seen, the two pressure distributions on the HLFC-panel are mostly on top of each other. Some minor deviations exist for $x/c < 0.2$, which is actually the most important region. The sectional pressure distributions on the NLF-panel are notably different, which is mainly due to the finite span.

Each section in this plot is represented with two lines, which is the port and the starboard side of the model. Since this is a symmetric case with $\beta = 0°$ and $\delta_R = 0°$, both sides should nominally have the same pressure distribution. The figure shows that this is true for all sections, except for the uppermost one $\eta = 0.92$. This very small asymmetry towards the tip of the VTP is basically a property of the backbone VTP model.

For future work these pressure distributions are now readily available as an input for stability analysis and transition prediction methods. Nevertheless, the present paper will focus on the experiments and the data processing and will therefore not cover such data exploitation.

The effective suction velocity distribution v_s on the panel is shown in Fig. 9 for the two sections $\eta = 0.47$ and 0.58 and for different plenum pressures $c_{p,P}$. The lines represent the v_s-distribution and the error bars indicate the uncertainty of the v_s-prediction process that was outlined in Sec. 2.3.2. Again, two lines are shown here for each case for both sides of the model. The waviness that was already identified in Fig. 6 is clearly visible and it also becomes clear that the waviness is not an uncertainty of the prediction, but a deterministic property. The two sections $\eta = 0.47$ and 0.58 are shown here in individual subfigures to avoid too many, overlapping lines; a detailed comparison between the two sections shows that the general distribution is very similar, but some deviations exist between the two sections which are basically a similar order of magnitude as the deviations between the two sides of the model.

It can be seen from Fig. 8 that the minimum pressure on the suction panel is at the rear end, i.e. at $x/c = 0.19$, and is $c_{p,\min} \approx 0.21$. Hence, for the case $c_{p,P} = -0.211$ the underpressure in the plenum is basically the same as in the outer flow, which leads to some transpiration, i.e. positive v_s-values, towards the rear end of the suction panel. Data is not shown here, but expectedly the transpiration becomes stronger if the plenum pressure $c_{p,P}$ is further reduced. Such cases are obviously not interesting for laminar flow control, since the transpiration will quickly trigger transition. Therefore, for the symmetric flow case at reference conditions, $c_{p,P} = -0.21$ is the minimum required plenum pressure.

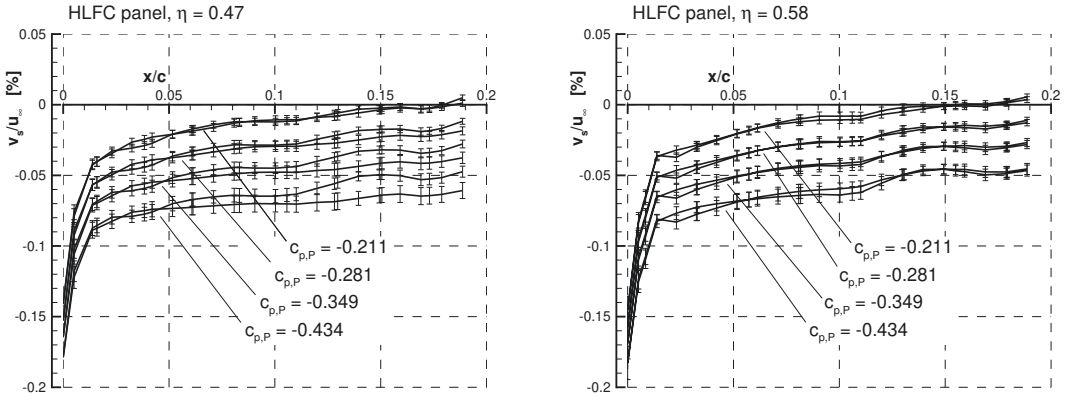

FIG 9. Estimated suction distribution v_s including uncertainty bounds σ_{v_s} for two sections on the HLFC-panel for the reference case $\beta = 0°$, $\delta_R = 0°$ at $Re = 22 \cdot 10^6$.

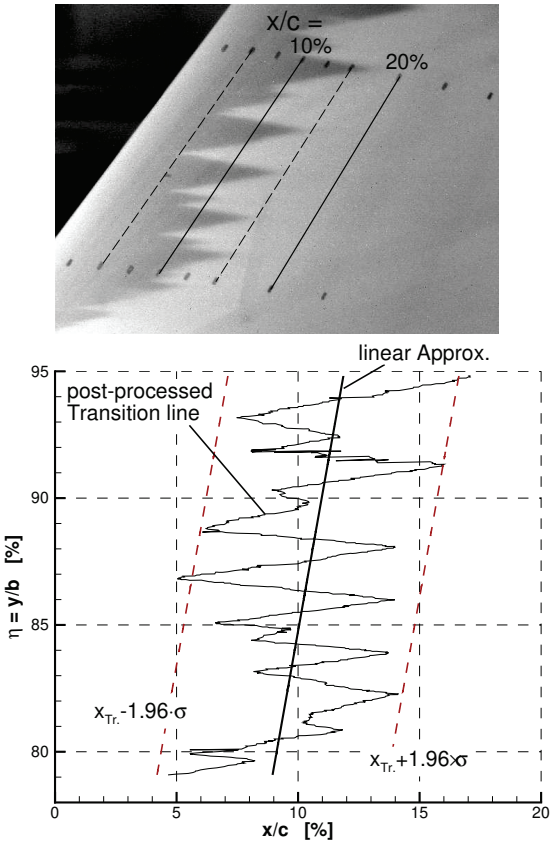

FIG 10. Postprocessing of Infrared images and linear regression along η, NLF-panel for the reference case $\beta = 0°$, $\delta_R = 0°$ at $Re = 22 \cdot 10^6$.

After having discussed the exemplary outcome of the c_p data fusion and suction velocity prediction, the following paragraphs will discuss the transition detection based on the infrared images.
First, Fig. 10 visualizes the process to evaluate the IR-images for the NLF-panel as an example. The raw image is shown here as-is, but for the analysis it is dewarped and a spatial calibration is defined as based on the tick marks. Then the transition line is identified from the contrast between the dark shaded areas (laminar region) and the brighter areas (turbulent region). This results in a raw transition line $(x_{Tr.}/c)(\eta)$, which is usually very rugged. The characteristic wedges that are clearly visible in Fig. 10 are either due to surface imperfections or are a result of a crossflow-dominated transition process. This can only be distinguished manually by comparing various images for e.g. different Re. For further analysis all regions that are turbulent, but that either do not respond to a change in the suction rate or that are obviously a result of a surface disturbance (turbulent wedge), are masked out and the remaining, rugged transition line is then approximated with a linear function. The lower part of Fig. 10 shows the rugged, raw transition line, the linear approximation and the 95 % confidence interval of the linear approximation. This approach finally gives a transition position $(x_{Tr.}/c)(\eta)$, which is independent from the exact appearance of the rugged transition line.
For the NLF panel, this process is relatively robust. For the HLFC panel, the process requires some manual, non-automatable tweaking, e.g. the masking of some regions. This, to a certain degree, makes the final results subjective.

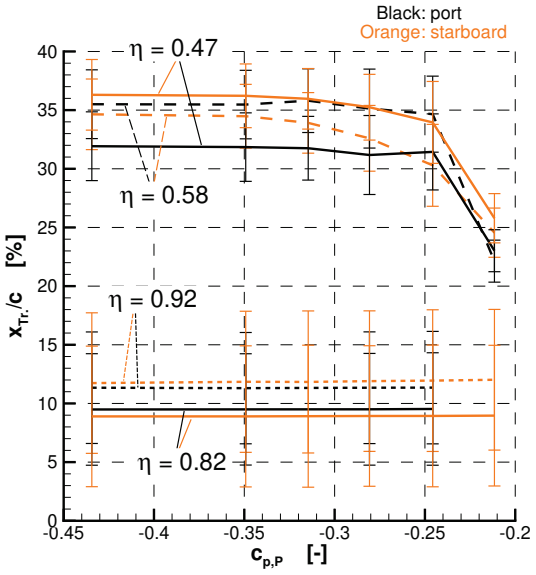

FIG 11. Transition positions for the reference case $\beta = 0°$, $\delta_R = 0°$ at $Re = 22 \cdot 10^6$; Error bars are the 95% confidence ($1.96 \cdot \sigma$) due to the rugged transition line

The outcome of the IR-Image analysis is highlighted in Fig. 11, again for the symmetric case at reference conditions. All lines in the lower region are the ones measured on the NLF panel. The other lines are the transition position downstream of the HLFC panel. For the NLF panel it can be seen that neither the transition position nor the confidence interval changes when the suction rate is varied. In fact, the IR images on the NLF panel are almost identical for all of the cases within a $c_{p,P}$-variation. It is consistently the case that the section $\eta = 0.82$ shows slightly earlier transition $x_{Tr.}/c$ than the section $\eta = 0.92$. Between these two section the pressure distribution is slightly different (as shown in Fig. 8), but also the Reynolds number of $\eta = 0.92$ is smaller due to the taper of the VTP planform. Both effects can likely explain the difference in the transition position.
For the transition positions downstream of the HLFC panel, the variations cannot be explained with such straightforward arguments. The pressure distributions are almost identical (ref. Fig. 8). The section $\eta = 0.58$ effectively sees lesser Reynolds number, due to smaller local chord length, but on the starboard side the transition (in a mean sense, ref. Fig. 10) is some percent of chord length earlier than at higher Re in $\eta = 0.47$. Herein, we have to interpret this difference as an additional uncertainty. In a thorough re-analysis of the cases with a transition prediction toolbox these observations can eventually

be explained with the local (small) differences in the pressure and suction velocity distribution (ref. Fig. 9). In the design of the suction system, [10], the effect of the suction was expected to level off for suction rates larger than $c_{p,P} \approx -0.35$, or $\Delta p \approx -2000\,\mathrm{Pa}$, respectively. This is also found in the present results. By design the suction system should be able to delay transition up to approximately $x_{Tr.}/c \approx 0.47$. In this wind tunnel entry, a laminar extent of approximately $x_{Tr.}/c \approx 0.35$ was actually achieved for these conditions.

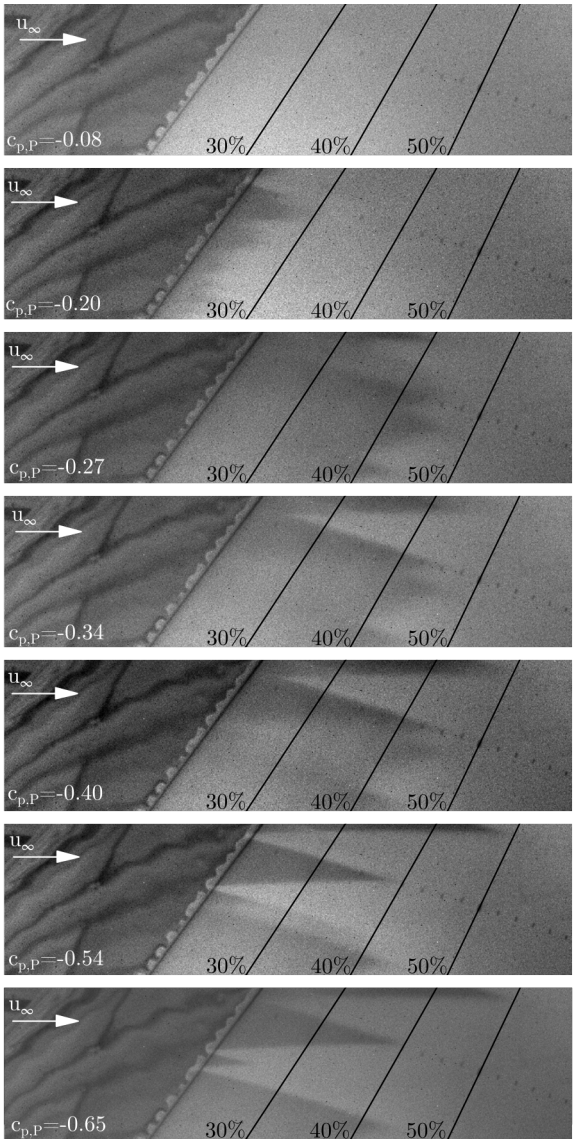

FIG 12. IR-images (port side, upper region of HLFC panel) for a case with reduced Re, $\beta = 0°$, $\delta_R = 0°$ at $Re = 18 \cdot 10^6$

To study the main sensitivities of the transition and of the LFC, a Reynolds number variation was done. While doing so, one interesting aspect was observed which will be discussed in Fig. 12: The imaged part is just behind the TSSD panel, at around $\eta \approx 0.6$–refer to Fig. 2 and 4 for better orientation. The TSSD panel itself can be seen as a dark, structured surface on the left side of the figures (the structures actually being the reflections of the wind tunnel side wall panels on the metallic surface). Remember that the metallic surface itself cannot be used to visualize the transition line.

The figure shows a variation of the plenum pressure, i.e. increasing suction strength from top to bottom, for a symmetric flow case at a slightly lower Reynolds number of $Re = 18 \cdot 10^6$. For the first four images ($c_{p,P} = -0.08 \cdots -0.34$) it can nicely be seen that–at first–increasing suction strength can increase the laminar region. At $c_{p,P} = -0.34$ the main transition line lies around $x_{Tr.}/c \approx 45\%$, which is larger than what is shown in Fig. 11 due to the smaller Reynolds number.

The interesting aspect is, that with further increasing suction strength, $c_{p,P} = -0.40$ and larger, some turbulent wedges appear. In the specific area imaged here, these wedges obviously emanate from the interface between the TSSD panel and the plain VTP surface. But in other locations, e.g. refer to [10], they also have some origin on the TSSD panel itself. It seems to be the case that with increasing suction, because the laminar boundary layer is further reduced in thickness, it becomes more prone to disturbances. In most cases we were able to trace the disturbance source from the turbulent wedges, e.g. to dents in the TSSD surface, imprints from the underlying structure or other obvious imperfections. Cleaning the disturbances however would have cost too much time and they were thus left as-is. In some cases–particularly on the interface between the TSSD-panel and the VTP backbone surface–these disturbances are rather small, e.g. small hair cracks in the putty used to blend the surfaces together. It seems that the combination of LFC and disturbances is still a challenging task.

4. SUMMARY AND OUTLOOK

A wind tunnel entry in DNW-LLF with a 4.45 m VTP was presented. A so-called TSSD suction system for laminar flow control was tested, which is a novel, tailored skin, single duct design, that would solve some of the practical problems yet existing with laminar flow control systems.

A data-fusion method was used to expand the pressure measured with discrete taps to the whole VTP surface. Then, the suction velocity distribution is predicted from the outer pressure distribution, the plenum pressure and a calibration of the pressure loss characteristics of the skin. Also, the total suction mass flow is measured with a high-accuracy mass flow meter. The accuracy of all elements of these processes was quantified and propagated. The mass flow meter is finally able to measure the total suction mass flow with an accuracy of $\pm 0.1\%$, the integrated suction velocity distribution has an uncertainty of around $\pm 0.9\,\%$ and agrees with the directly measured mass flow within approximately $+0.5\,\%$.

For the analysis of the transition line from the infrared images, herein we fitted a (piecewise) linear approximation line to smooth out the rugged appearance.

The “ruggedness” of the transition line, i.e. chordwise variations along span, can be as much as $10\,\%$ chord. For the symmetric flow case the agreement of the final transition position $x_{Tr.}/c$ between both (nominally identical) sides is typically around $3\,\%$ to $5\,\%$.
For the symmetric case under reference conditions a laminar length of $x_{Tr.}/c \approx 0.34$ was achieved, while the VTP without suction would be fully turbulent. The required suction velocities, and plenum pressures, respectively, agree good with the design data shown in [10]. The laminar length is shorter than what was predicted under ideal conditions, nevertheless the system is able to retain a significant amount of laminar boundary layer flow over the VTP even at high Re.
The TSSD system therefore seems to be an interesting approach to an exchangeable, large-scale manufacturable suction system design. However, this experiment has not yet fully succeeded in creating a surface without disturbances and waviness, and this still needs to be solved on the way to industrial application.
The next step would be to re-analyse the measured cases with a suitable transition prediction toolbox. All necessary input data is available from the experiments and the data fusion process: (i) Pressure distributions that can be extracted in more-or-less arbitrary sections, (ii) suction velocity distributions, also in arbitrary sections, (iii) Transition position downstream of the HLFC-Panel as well as on the NLF reference panel. Each of these datasets not only covers the mean data, but also standard deviations and/or uncertainty bounds. Therefore, it would be most consistent to also embed the transition prediction into a suitable probability analysis environment, such as a Monte-Carlo approach.
Speaking from the data analysis that we did so far, one challenging part in such an approach will likely be the transition position evaluation: Because of some small disturbances, determining the transition position requires manual masking, blanking and post processing and is therefore to some extent subjective. This might finally result in a rather broad range of critical N-factors.

Acknowledgements

This project has received funding from the Clean Sky 2 Joint Undertaking (JU) with project “Advance Laminar Flow Control with Variable Porosity (ALVAR)” under grant agreement No. 882646. The conceptual and aerostructural design as well as the manufacturing of the TSSD leading edge is part of the Clean Sky 2 project “New Aircraft Configurations and Related Issues (NACOR)” under grant agreement No. 945521.
The authors deeply acknowledge the support from
- Philipp Mühlmann, German Aerospace Center (DLR), Institute of Aerodynamics and Flow Technology, who supported the IR-image analysis,
- Sven Schaber, AIRBUS Operations GmbH, who supported the local porosity measurements,
- Bodo Mickan, the National Metrology Institute (PTB), working group 1.43 “high pressure gas”, who supported the calibration of the master flow meter
- Ulrich Römer, TU Braunschweig, Institut für Dynamik und Schwingungen, who supported the uncertainty quantification and propagation analysis.
- A. Bertram, P. Bekemeyer and J. Himisch, German Aerospace Center (DLR), Institute of Aerodynamics and Flow Technology, who supported application of the data fusion toolbox “SMARTy”.

Contact address:

P.Scholz@tu-braunschweig.de

References

[1] Nils Beck, Tim Landa, Arne Seitz, L.M.M. Boermans, Y. Liu, and Rolf Radespiel. Drag Reduction by Laminar Flow Control. *Energies*, 252(11):1–28, 2018. DOI: 10.3390 /en11010252.

[2] Stanislav Karpuk, Rolf Radespiel, and Ali Elham. Assessment of Future Airframe and Propulsion Technologies on Sustainability of Next-Generation Mid-Range Aircraft. *Aerospace*, 9(5):279, May 2022. DOI: 10.3390/aerospace9050279.

[3] Ronald D Joslin. Aircraft Laminar Flow Control. *Annual Review of Fluid Mechanics*, 30:1–29, 1997. DOI: 10.1146/annurev.fluid.30.1.1.

[4] G. Schrauf. Status and perspectives of laminar flow. *The Aeronautical Journal*, 109(1102):639–644, December 2005. DOI: 10.1017/S000192400000097X.

[5] Aaron A. Tucker, Helen L. Reed, William S. Saric, and Donald T. Ward. Design of Experiments with an Application to Laminar Flow Control Flight Research. In *AIAA Atmospheric Flight Mechanics Conference*, San Diego, California, USA, January 2016. American Institute of Aeronautics and Astronautics. DOI: 10.2514/6.2016-1758.

[6] C.-H. Rohard and Arne Seitz. Simplified-HLFC/ Entwurf eines Seitenleitwerks mit Hybrid-Laminarhaltung für den Airbus A320. In *60. Deutscher Luft- Und Raumfahrtkongress*, Bremen, September 2011.

[7] Michelangelo Corelli Grappadelli, Peter Scholz, Rolf Radespiel, and Camli Badrya. Experimental Investigations of Boundary Layer Transition on a Flat-Plate with Suction. In *AIAA SciTech Forum*, Virtual event, January 2021.

[8] Matthias Horn, Arne Seitz, and Marvin Schneider. Novel tailored skin single duct concept for HLFC fin application. In *7th European*

Conference for Aeronautics and Space Sciences (EUCASS), Mailand, Italy, July 2017. DOI: 10.13009/EUCASS2017-44.

[9] Marvin Schneider, Matthias Horn, Stefan Ritt, and Arne Seitz. Structural Design and Testing of a Tailored Skin Single Duct (TSSD) Fin Application. In *31st Congress of the International Council of the Aeronautical Sciences (ICAS)*, page 8, Belo Horizonte, Brasil, September 2018.

[10] A Seitz, M Horn, A Barklage, P Scholz, C Badrya, and R Radespiel. Wind Tunnel Verification of Laminar Boundary Layer Control TSSD Concept. In *AIAA Aviation Forum and Exposition*, page 16, Chicago, USA, June 2022. DOI: 10.2514/6.2022-3552.

[11] Matthias Horn, Heiko Frhr. von Geyr, Thomas Weddig, J Bruns, and M Schradick. Auslegung, Fertigung und Funktionsdemonstration einer HLFC Leading Edge. In *Deutscher Luft- und Raumfahrtkongress 2016*, page 12, Braunschweig, September 2016.

[12] T. Kilian and M. Horn. Verification of a chamberless HLFC design with an outer skin of variable porosity. *CEAS Aeronautical Journal*, 12(4):835–845, November 2021. DOI: 10.1007/s13272-021-00528-4.

[13] Alexander Barklage, Ulrich Römer, Philipp Bekemeyer, Anna Bertram, Jan Himisch, Rolf Radespiel, and Camli Badrya. Analysis and uncertainty quantification of a hybrid laminar flow control system. In *AIAA SCITECH 2022 Forum*, San Diego, USA, January 2022. DOI: 10.2514/6.2022-2452.

[14] Alexander Barklage, Ulrich Römer, Arne Seitz, Matthias Horn, Rolf Radespiel, Peter Scholz, and Camli Badrya. Uncertainty analysis of the laminar boundary layer control TSSD concept. In *AIAA Aviation Forum and Exposition*, page 20, Chicago, USA, June 2022.

[15] Zhong-Hua Han, Stefan Görtz, and Ralf Zimmermann. Improving variable-fidelity surrogate modeling via gradient-enhanced kriging and a generalized hybrid bridge function. *Aerospace Science and Technology*, 25(1):177–189, March 2013. DOI: 10.1016/j.ast.2012.01.006.